Aalto University

Speck, Florian D.; Ali, Farhan SM; Paul, Michael T. Y. ; Singh, Ramesh K. ; Böhm, Thomas ; Hofer, André; Kasian, Olga ; Thiele, Simon ; Bachmann, Julien ; Dekel, Dario R. ; Kallio, Tanja; Cherevko, Serhiy

Improved Hydrogen Oxidation Reaction Activity and Stability of Buried Metal-Oxide Electrocatalyst Interfaces

Improved Hydrogen Oxidation Reaction Activity and Stability of Buried Metal-Oxide Electrocatalyst Interfaces

Florian D. Speck,* Farhan S. M. Ali, Michael T. Y. Paul, Ramesh K. Singh, Thomas Böhm, André Hofer, Olga Kasian, Simon Thiele, Julien Bachmann, Dario R. Dekel, Tanja Kallio, and Serhiy Cherevko*

Cite This: *Chem. Mater.* 2020, 32, 7716−7724
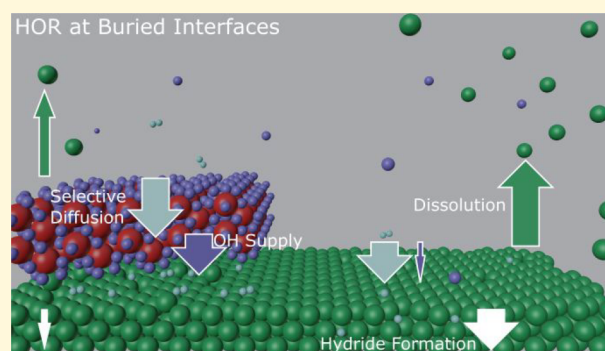
Read Online

ACCESS | Metrics & More | Article Recommendations | Supporting Information

ABSTRACT: Various bifunctional metal-oxide composites have recently been proposed as advanced hydrogen oxidation reaction (HOR) electrocatalysts for anion-exchange membrane fuel cells (AEMFCs). It is postulated that metal and oxide are active sites for the adsorption of hydrogen/proton and hydroxide ions, respectively. Of particular interest are the so-called buried interfaces. To investigate processes governing activity and stability at such interfaces, we prepare model Pd and Pt electrocatalysts which are fully covered by thin CeO_x films. We investigate how oxide thickness influences HOR activity and dissolution stability of the electrocatalysts. It is found that materials behave very differently and that only Pd exhibits an enhanced HOR activity, while both oxide-protected metals are more stable toward dissolution. A 10-fold decrease in dissolution and 15-fold increase in HOR exchange current density are demonstrated for the optimized Pd/CeO_x composites in comparison to pure Pd. We assess the mechanism of the electrocatalytic improvement as well as the role of the protective oxide films in such systems through advanced electrochemical and physical analysis. It is highlighted that a uniform, semipermeable oxide layer with a maximized electrocatalyst−oxide interface is crucial to form HOR catalysts with improved activity and stability.

INTRODUCTION

Anion-exchange membrane fuel cells (AEMFCs) are often positioned as an advantageous fuel cell technology, which offers a stable operational environment even for platinum group metal (PGM) free electrocatalysts.[1−3] The use of such catalysts will potentially result in a significantly reduced investment cost if compared to the competing proton-exchange membrane fuel cell (PEMFC) technology. Alkaline media, however, come with a significant drawback—the anodic hydrogen oxidation reaction (HOR), even on PGM materials, is considerably slower than in acidic media.[2,4,5] Thus, HOR catalysts need to be optimized when moving toward AEMFCs.

State-of-the-art PGM-free cathode catalysts, such as Fe−N−C, have shown comparable or even higher activities than PGM catalysts,[6] despite the 4e− reduction of O_2 in alkaline media being more sluggish than the 2e− oxidation of H_2.[7,8] For the HOR, on the other hand, PGM-free catalysts are rare.[4,9] Currently, the most promising PGM-free alternatives are Ni-based catalysts that are often alloyed or mixed with other non-PGMs to improve catalytic properties of the oxophilic Ni.[10−12] The HOR activity of such catalysts is still prohibitively low for any commercial application, despite recent reports of promising results. Another shortcoming of the current Ni-based HOR catalysts is of intrinsic thermodynamic character—at higher anodic potentials during high load operation,

dissolution of alloying elements and irreversible Ni oxidation and passivation may take place.[13]

Such circumstances lead to the realization that, for the time being, AEMFCs still need to rely on PGM-based HOR catalysts. Nevertheless, even though PGMs cannot be completely replaced, their amount can be minimized. The latter can be achieved by the development of more active catalysts. The HOR kinetics of Pt in acid is nearly ideal in terms of the volcano-relation.[14−16] Thus, in PEMFC, potential losses of 10 mV and less during high load operation are possible with Pt/C based anode catalysts of 0.05 mg_{Pt}/cm^2.[17] On the other hand, the same catalyst displays a HOR-activity that is orders of magnitude lower in an alkaline environment.[3,18] Currently, significantly higher PGM loading (typically PtRu alloys) is required to reach power densities of more than 1 W cm^{-2}.[19,20] Furthermore, transient dissolution of the Pt and Ru anode catalysts (oxidation when in contact

with air, followed by reduction during start-up) affects the long-term stability especially at high pH.[21,22]

Recently, the beyond 1 W cm^{-2} performance of AEMFC was achieved with a Pd-based anode electrocatalyst.[19] This power density was achieved through the addition of CeO$_x$ as a second, oxophilic component, and further by mixing the Pd-CeO$_x$ composite with a carbon support to improve catalyst utilization and catalyst layer conductivity.[23,24] Interestingly, the Pd-CeO$_x$/C composite exhibited unprecedented stability against dissolution,[25] even though Pd itself is less stable than Pt in alkaline environments.[22] These new results demonstrate that simultaneously active and stable catalysts are accessible and that further optimized materials may be possible. However, the underlying mechanism of the increased Pd-CeO$_x$/C performance needs to be understood to reach this goal. Unfortunately, the high complexity of this catalyst system is a significant obstacle for fundamental mechanistic studies.[25] Indeed, despite several attempts to prepare various interfaces between Pd, CeO$_x$, and C through versatile synthesis approaches,[25−29] it is still uncertain how this activation of Pd toward HOR goes hand in hand with decreased Pd dissolution and how the ideal interface (between Pd and CeO$_x$ but also other catalyst/cocatalyst materials) should be designed. To overcome these shortcomings of 3D-catalyst architectures, a simplified 2D-catalyst model system is presented in this work.

Assuming that the HOR takes place at the Pd-CeO$_x$ interface (bifunctional mechanism), this interface needs to be maximized in real systems to achieve higher performances. Hypothesizing further and assuming that the reduced dissolution of Pd is due to physical blockage (e.g., diffusion barrier) by CeO$_x$, it is clear that such protection needs to be enhanced in order to reach high catalyst longevity at low catalyst loadings. In our opinion, the closest system to simulate such an interface is a catalyst covered with a semipermeable layer. Such buried electrocatalytic interfaces are known in electrocatalysis and photoelectrochemistry.

It was recently shown that the reaction selectivity can be tuned by modifying the catalyst surface. Indeed, modified electrodes were previously investigated in acidic environment to tune the HOR selectivity of anode catalysts. A low ORR activity of anode catalysts was demonstrated by depositing semipermeable surface layers of organic or oxidic character.[30−34] The latter finding implies that such a catalyst in the anode would eliminate high anodic potentials on the cathode during start/stop cycles on the system level.[30−33,35,36] The formation of an oxidic passivation layer was also suggested as an explanation for the deteriorated ORR activity of oxide supported Pt catalysts.[37,38] Recently, it was demonstrated that the activity and stability of Pt and Pt-based ORR catalysts can also be improved by modification with ionic liquids.[39,40] The mechanism of this improved performance, however, is still under debate.

In this work, we propose a model of a quasi-2D buried electrocatalytic interface system with a well-controlled overlayer thickness in order to study both activity and stability simultaneously on a fundamental level. This model simplifies the complex 3D structure of real Pd-CeO$_x$/C catalysts. The system was realized by using atomic layer deposition (ALD) to deposit CeO$_x$ overlayers of different thicknesses onto flat Pd surfaces, thus forming CeO$_x$@Pd interfaces. For the sake of comparison, also CeO$_x$@Pt interfaces were prepared and studied. It is found that both high HOR activity and a

significant decrease in Pd dissolution can be achieved for CeO$_x$@Pd.

■ EXPERIMENTAL SECTION

Film Deposition. Thin-film synthesis started with Si(100) wafers that were precleaned in an ultrasonic bath with acetone and isopropanol (1:1), rinsed with ultrapure water and dried with compressed dry air. Using electron beam evaporation in a high vacuum chamber (BesTec GmbH), a 20 nm Ti adhesion layer was deposited first. Then, PGMs were deposited from Pt or Pd pellets (99.99%, Kurt J. Lesker company) at a chamber pressure of 2×10^{-6} Pa. During deposition, the substrate was rotated with 20 rpm at room temperature. Under these conditions, 200 nm films of Pt and Pd were deposited at a rate of 2 and 1 Å s^{-1}, respectively.

Atomic layer deposition (ALD) was used to deposit CeO$_x$ layer onto Pt or Pd films. Five different ALD deposition cycle amounts (4, 8, 12, 16, and 20) were chosen to vary CeO$_x$ thickness. In the following, the nomenclature is M-Ce$_N$, where N is the number of ALD cycles and M is the metal on which CeO$_x$ was deposited. The ALD was carried out in a commercial hot-wall cross-flow F120 ALD reactor (ASM Microchemistry Ltd.) using a 2,2,6,6-tetramethyl-3,5-heptanedionate (thd) cerium complex as a precursor and ozone as an oxidizer. Ce(thd)$_4$ was prepared from Ce(NO$_3$)$_3 \times$ 6 H$_2$O (≥98.5%, Merck), and thd (≥97%, Tokyo Chemical Industry), while the ozone was supplied by a laboratory ozone generator (model 502, Fischer) using oxygen (5.0). A single ALD cycle consisted of four steps:

  I   Ce(thd)$_4$ was evaporated at 140 °C in the precursor chamber and pulsed for 4 s into the reaction chamber at 2−3 mbar to adsorb on the heated substrate at 275 °C.

 II   Purging the reaction chamber for 8 s with N$_2$ (5.0) to remove precursor residue.

III   Oxidizing the adsorbed precursor for 3 s in O$_3$.

IV   Purging the chamber from side products and O$_3$ through a 10 s N$_2$ (5.0) purge.

Physical Analysis of Thin Films. All samples underwent identical X-ray photoelectron spectroscopy (XPS) analysis in a PHI Quantera II system (Scanning XPS Microprobe, Physical Electronics), operated with Al Kα irradiation at 50 W and 15 kV. Survey ($\Delta E = 1$ eV) and high resolution ($\Delta E = 0.25$ eV) region spectra (Pt/Pd, Ce, O, and C) were measured with a dwell time of 100 ms and a pass energy of 280 and 140 eV, respectively. The surface region was further probed by tilting the sample, so only photoelectrons escaping at the angle ρ were analyzed. Here, spectra were gathered at 85° to the surface normal, with identical X-ray settings. Analysis of the angle-resolved spectra was done according to eqs S1 and S2.

Furthermore, to verify the physical presence of CeO$_x$ thin films on Pt and Pd substrates focused ion beam milling (FIB) in a scanning electron microscope (SEM) and transmission electron microscopy (TEM) were performed. Sections of oxide-coated substrate were lifted from the sample through the use of a Zeiss Crossbeam 550 (Zeiss GmbH, Germany). These sections were lifted from the sample, thinned, and finally analyzed in a TEM. The general lamella lift-out procedure was performed as follows: a 500 nm thick Pt protection layer was deposited in situ onto the sample by electron beam induced deposition over the intended area of milling. A subsequent 2 μm thick Pt layer was deposited by FIB inducted deposition directly on top of the e-beam deposited Pt. An area of approximately 10×3 μm^2 was covered by the Pt protection layer. A lamella of approximately $8 \times 1 \times 5$ μm^3 (width × length × depth) was lifted from the center of the Pt covered area by the FIB-SEM with an operating FIB acceleration voltage of 30 kV using a Kleindik MM3A-EM micromanipulator (Kleindiek Nanotechnik GmbH, Germany). The lifted lamella was attached to a Cu Omniprobe lift-out grid (Plano GmbH, Germany). The attached lamella was thinned with the FIB at 30 kV to a thickness of ∼500 nm. The lamella was then further polished to a thickness of ∼50 nm with the FIB operating at 10 kV. The polished lamella was then transferred to a TEM for imaging and elemental identification. Samples of thinned lamellas were analyzed by a Titan Thermis TEM (Thermo Fisher, U.S.A.) operating at 300 kV under scanning
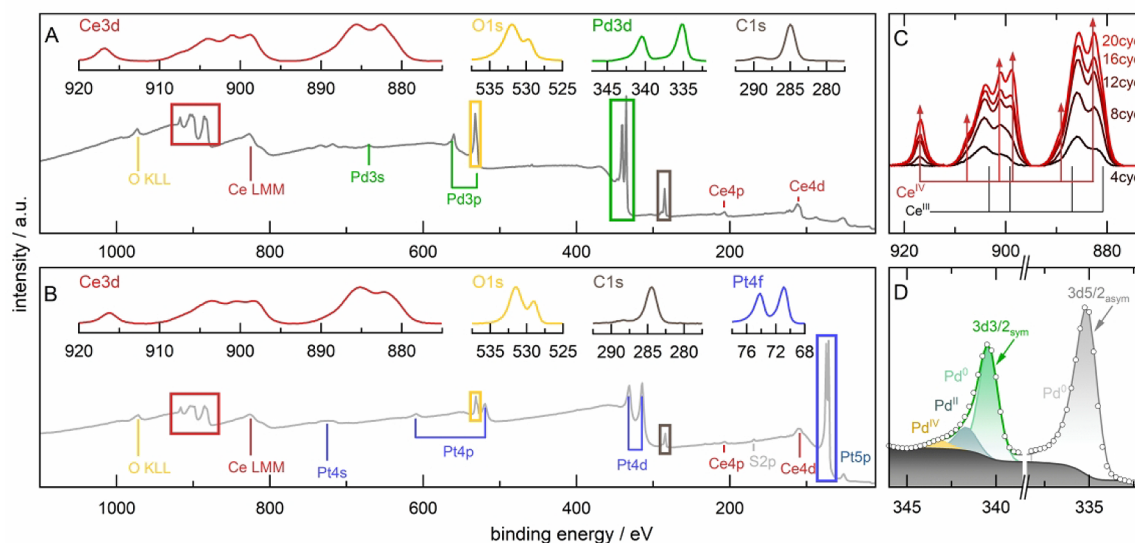
Figure 1. Summarized XPS analysis of Pd−Ce$_{20}$ (A) and Pt−Ce$_{20}$ (B). Detailed evolution of the Ce 3d spectral region with increasing film thickness on top of Pd (C). Exemplary fit components of the Pd 3d$_{5/2}$ spectra using a single asymmetric fit function and the Pd 3d$_{3/2}$ region fitted with symmetric peaks for all three oxidation states (D). Fit analysis was done for a representative Pd−Ce$_{20}$ sample and is further explained in the supplementary XPS discussion.

transmission electron microscopy (STEM) mode with a high angle annular dark field (HAADF) detector. The samples were mounted and inserted into the TEM by a double tilt holder. To ensure an in-plane viewing orientation of the CeO$_x$ thin films, the lamella was oriented by aligning the zone axis of the underlying Si (110) substrate. Energy-dispersive X-ray spectroscopy (EDX) information was collected by a Super-X EDX detector. The obtained results were analyzed and processed by Velox version 2.8 (Thermo Fisher, U.S.A.).

The surface morphology was also tracked with atomic force microscopy (AFM) on a WITec alpha 300 R microscope, operated in contact mode. Images were generated from scanning a 0.5 × 0.5 μm^2 area at a scan speed of 0.25 $\mu m\ s^{-1}$ and at a pixel pitch of 5 nm. Three images per sample were obtained and corrected for sample tilt by a linewise slope subtraction. Sample roughness as a descriptor between the different samples was averaged through the arithmetic mean height deviation (R_a) from the three images.

Using spectroscopic ellipsometry (SENpro by Sentech Instruments GmbH), film thicknesses of all samples were determined from a fitting model based on the thickest CeO$_x$ films. Measurements were performed between 370 and 1050 nm at an incident angle of 70°. Mean squared errors between 0.8 and 3.5, indicate a nonideal system and the determined thicknesses can only be seen as an approximation.

The four-point probe resistivity measurement system is based on a homemade probe head, developed at Technion. The distance between the contacts is 2.17 mm. The system includes a Keithley Ke2400 measuring instrument and software written in LabVIEW. The resistance given in Ω is measured through the conductive layer.

Electrochemical Methods. Electrocatalytic activities of M$_N$-films toward HOR and ORR were determined using a custom-made Teflon rotating disk electrode (RDE) cell. The cell was cleaned rigorously before measurements. Initially, a boiling step in dilute HClO$_4$ was performed, followed by storage in acidified, saturated KMnO$_4$ solution overnight. Before use, the cell was rinsed with dilute H$_2$O$_2$ solution, washed until neutral pH was achieved, and boiled four times in water. Between experiments with the same material, the cell was boiled in water twice.

An RDE modified to handle 5 × 5 mm silicon wafer pieces (SiRDE) was used to study M$_N$-films prepared on silicon wafers. A modification of a recently reported approach was used in this work.[41] A schematic of the employed SiRDE is shown in Figure S1. Double-sided copper tape was folded around the wafer's edges to make contact with the catalyst film and then attached to the center of a homemade glassy carbon (GC) RDE tip. A circular Kapton tape with

a hole (D = 2 mm) in the center was cut using a laser cutter (LaserPro Spirit, GCC) and used to cover the Cu tape as well as the GC, leaving only an exposed catalyst area of 0.0314 cm^2. The tip was then immersed in the RDE cell filled with 30 mL of 0.05 M NaOH (99.99% Suprapur, Merck) electrolyte. The latter was prepared by dissolving NaOH in H$_2$O (18.2 MΩ, Milli-Q IQ700, Merck). An Ag/AgCl (3 M KCl, Methrom) and graphite rod (99.995%, Sigma-Aldrich) were used as reference and counter electrodes. All potentials are presented on the reversible hydrogen electrode (RHE) potential scale. The RHE was measured daily on a commercial Pt RDE (Pine) to calibrate the Ag/AgCl reference electrodes. The potential was controlled with a potentiostat (Reference 600, Gamry). After electrochemical cleaning cycles, when the Ar purged cyclic voltammo-grams (CVs) superimposed each other, the uncompensated resistance was measured by electrochemical impedance spectroscopy (EIS). All data on HOR and ORR activity are compensated for this resistance. The obtained linear sweep voltammograms (LSV) are additionally smoothed with a 10 point FFT filter function of OriginPro 2019. Kinetic analysis was done according to the Butler−Volmer equation, by fitting the linear region of a Tafel plot.

Catalyst stability was evaluated by using an electrochemical scanning flow cell (SFC) connected online to an inductively coupled plasma mass spectrometer (ICP-MS) (NexION 350x, PerkinElmer). Details on this setup can be found elsewhere.[42] Briefly, it allows quantification of dissolved M^{n+} species during electrochemical tests and provides time- and potential-resolved dissolution analysis. The same electrolyte and electrodes were used as in the above activity studies. The ICP-MS was calibrated daily for the detection of Pt^{n+}, Pd^{n+}, and Ce^{n+} species using four calibration standard solutions (Pt, Pd, and Ce, with 0, 0.5, 1, and 5 $\mu g/L$, Centripur, Merck).

■ RESULTS

One of the main scientific objectives of this work was to investigate the effect of a CeO$_x$ layer on the catalytic performance of Pt and Pd catalysts. Thickness, composition, structure, and morphology of the layers prepared with different numbers of ALD cycles were estimated, using a set of physical characterization techniques including XPS and ARXPS, cross-sectional TEM, AFM, and ellipsometry.

First, the oxidation state and composition of the surface region were studied by XPS. The obtained results for all
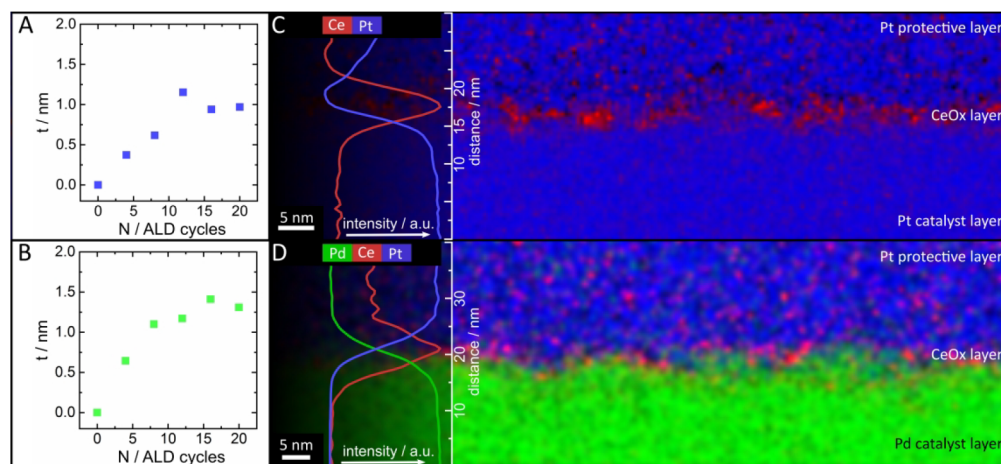
Figure 2. CeO$_x$ film thickness depending on the number (N) of ALD cycles of Pt–Ce$_N$ (A) and Pd–Ce$_N$ (B). Cross-sectional TEM images of Pt–Ce$_{20}$ (C) and Pd–Ce$_{20}$ (D) with insets of the normalized average EDX intensity per pixel row.

samples are summarized in Table S1, and representative survey spectra for 20 ALD cycles of CeO$_x$ deposition (Pd–Ce$_{20}$ and Pt–Ce$_{20}$) are shown in Figure 1A,B. High-resolution spectra for Ce (red), O (yellow), Pd (green) or Pt (blue), and C (gray) are visualized as insets.

For Pd–Ce$_{20}$, besides C impurities and O, one can clearly see the XPS signal from Ce, confirming its successful deposition. Interestingly, the XPS signal from Pd is still very strong, despite a relatively high number of ALD deposition cycles. The Ce/Pd atomic ratio for the thickest CeO$_x$ layer is still 30%/70%. As expected, this ratio decreases further with a decreasing number of deposition cycles (see Figure 1C and Table S1).

As highlighted by arrows in Figure 1C, besides the change in the amount of Ce, there is also a clear trend in the transition from a partially reduced Ce^{III}O$_x$ (Pd–Ce$_4$) to fully oxidized Ce^{IV}O$_x$ (Pd–Ce$_{20}$) state with deposition cycles.[43] There are two explanations for this effect: (a) faster reduction of thin ceria layers due to the instrument's sputter neutralization;[44] (b) interfacial effect of partial charge transfer from Pd to CeO$_x$. To investigate this effect further, the Pd 3d region was analyzed in detail. Due to existing ambiguities in the Pd peaks fitting (Figure 1D) and data interpretation, a solid conclusion on the existence of partial charge transfer from Pd could not be drawn (see the discussion in SI). However, Figure S2 suggests that there are no changes in the Pd 3d or Pt 4f regions with increasing CeO$_x$. The same observations regarding impurities, increasing CeO$_x$ coverage, and PGM oxidation state were made for CeO$_x$ covered Pt (Figure 1B and Table S1).

The thickness of CeO$_x$ films on all samples was estimated using three different methods. Results obtained from angle-resolved (AR)XPS are shown in Figure 2A,B. According to this method, the equivalent thickness increases gradually and reaches ca. 1.0 and 1.3 nm for Pt and Pd, respectively. Further, films with the highest amount of CeO$_x$ were analyzed by EDX from cross-sectional TEM, with images for Pt–Ce$_{20}$ and Pd–Ce$_{20}$ shown in Figure 2C,D. Here, the protective layer applied during sample preparation by the FIB-SEM includes some Ce, possibly due to the invasive process of milling. The insets on the left side show the intensities of the Lα emission lines of the relevant elements averaged over one row of pixels in the whole picture. The thicknesses of 2.2 ± 0.3 and 5.5 ± 0.5 nm for Pt–Ce$_{20}$ and Pd–Ce$_{20}$, as estimated from the fwhm of the Ce

intensity peaks, are significantly higher than that from ARXPS. As a third measure of film thickness, ellipsometry was conducted. The results are summarized in Figure S3. Thicknesses from ellipsometry are similar to those from TEM.

The deviation in the thicknesses measured with ARXPS, TEM, and ellipsometry can be related to the surface roughness (R_a) of the initial Pt/Pd substrate. Therefore, AFM was used to investigate the R$_a$ of these films. Figures S4 and S5 reveal that the surface of the sputtered film has a R_a(Pt) = 1.48 ± 0.04 nm. An increase in CeO$_x$ coverage lowers this surface roughness to R_a(Pt–Ce$_{20}$) = 0.81 ± 0.01 nm (compare Figure S5) due to preferential deposition in valleys, in line with what we see in TEM cross sections (Figure 2C,D). Therefore, these three complementary methods show a gradual increase in the oxide layer thickness by increasing the number of ALD cycles. Based on these results, we conclude that the true film thickness lies between min/max values obtained by these different techniques, and the films are likely porous.

As briefly discussed in the Introduction, the addition of CeO$_x$ to Pd/C increases its catalytic activity toward the HOR.[24−26] Several strategies have been proposed to improve this activity further, i.e., by changing the CeO$_x$ to Pd ratio, the amount of conductive carbon support, modifying CeO$_x$ with Pd, or vice versa, etc. It was found in these studies that the electrocatalytic activity can be improved. Still, the exact role of CeO$_x$ remains elusive, especially when the surface of Pd is blocked with CeO$_x$. However, by adding an oxidic layer with varying thickness, the conductivity needs to be addressed first (especially in 3D systems). Therefore, four-point probe measurements were conducted and are summarized in Table S2. No discernible impact of layer thickness was observed, suggesting that these nanoscaled layers do not lower electrocatalytic activity through conductivity issues.

The physical analysis revealed that by controlling the number of ALD cycles, we could control the thickness of CeO$_x$, hence forming an ideal system to investigate the phenomenon of electrocatalytic improvement. This 2D system is also suited to investigate the reported selectivity of HOR when oxygen is present in the electrolyte. For this, HOR and ORR were studied on the CeO$_x$@Pt and CeO$_x$@Pd electrodes of varying CeO$_x$ thicknesses. As a benchmark, the polycrystalline Pt electrode was used.[45] Figures 3A and B present HOR results for CeO$_x$@Pt and CeO$_x$@Pd electrodes, respectively.
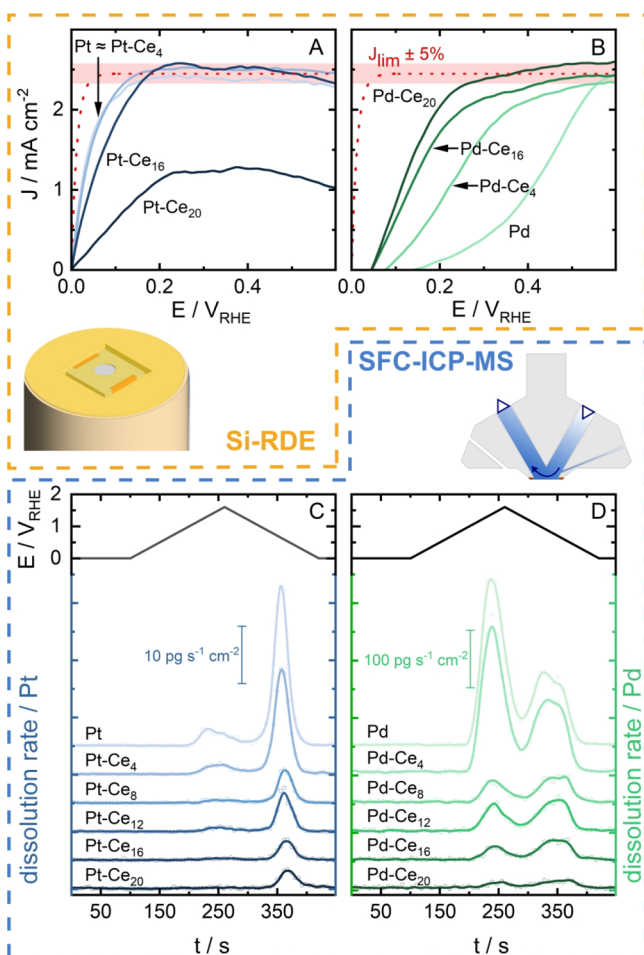
Figure 3. HOR activities of select Pt−Ce$_N$ (A) and Pd−Ce$_N$ (B) (N = 0, 4, 16, and 20) in H$_2$ saturated 0.05 M NaOH through LSV scanning from more positive potentials at a scan rate of 20 mV s^{-1}. Dissolution rates over time of sputtered Pt (C) and Pd (D) wafers with different ALD coverages of CeO$_x$. Smoothed dissolution data during a slow CV experiment in H$_2$ saturated 0.05 M NaOH from 0 to 1.6 V$_{RHE}$ (black) at a scan rate of 10 mV s^{-1} is shown as a solid line with original data shown as hollow circles.

The theoretical diffusion-limited current derived from the Levich equation is shown in dotted red with a pale red error bar, reflecting typical errors of its estimation.[46] A full kinetic analysis with every sample corresponding activity descriptors can be found in Table S3.

Pt is known to be very sensitive to trace amounts of impurities in the electrolyte blocking active sites,[46] but the activity toward the HOR is not impacted negatively by covering the surface with thin layers (N < 12) of CeO$_x$. Indeed, half-wave potentials ($E_{1/2}$), which are used as a visual descriptor of HOR activity, remain unaffected within measurement accuracy. The highest exchange current density (j_0) was measured for the Pt−Ce$_8$ sample (see Table S3). At a coverage of $N \geq 12$, $E_{1/2}$, j_0, and even the limiting currents start to degrade.

Bare Pd is known to bind hydrogen too strongly and to form hydrides at low potentials (PdH$_x$).[1,14,15] In terms of the HOR, this is evidenced in Figure 3B by the transition from limiting anodic HOR currents to cathodic currents at rather high HOR overpotentials. This transition to cathodic currents at 0.18 V$_{RHE}$ shifts closer to the theoretical H$_2$/H$_2$O couple with

increasing amounts of CeO$_x$ ALD cycles. $E_{1/2}$ decreases drastically by more than 200 mV already for 4 ALD cycles of CeO$_x$. With the application of additional ALD cycles, the decrease in $E_{1/2}$ proceeds with 40−10 mV per sample (Table S3). The maximized HOR activity is achieved for the thickest CeO$_x$ film studied, which was comprised of 20 ALD cycles and a thickness of ca. 1.3 nm according to ARXPS. Here, we measure exchange current densities (j_0 = 1.05 mA cm^{-2}) 15 times higher than that of bare Pd (j_0 = 0.07 mA cm^{-2}) and close to that of our benchmark, Pt (j_0 = 1.27 mA cm^{-2}). Our measurements are in good correlation with literature values for the bare metals dispersed on carbon in 0.1 M NaOH.[47]

The impact of the CeO$_x$ coverage on the ORR is presented in Figure S6. For all CeO$_x$ covered samples, the activity of the blank PGM samples was not reached and degraded gradually. Reduced activity is shown by a shift in onset potential, and at high coverages even a reduced limiting current suggesting either a less than 4 e$^-$ process, or an actual O$_2$ diffusion barrier as suggested by the hypothesis of a semipermeable character of the CeO$_x$ layer.[34] Therefore, deactivation toward the ORR is supposed to increase lifetime by simply lowering the open circuit potential upon shutdown in real devices. However, when assuming that the semipermeable film blocks relatively large O$_2$ molecules from passing, one should also assume that the same is true for large PGM ions. In this context, we subjected all samples to online ICP-MS stability tests.

The dissolution behavior of both investigated PGMs (Pt and Pd) in aqueous electrolytes are well described in the literature, and our results on the blank metals shown in Figure 3C,D are analogous to the previous findings on polycrystalline metals.[21,22,25,48,49] Thus, we focus on how the presence of oxide overlayers affect the dissolution. Moreover, for the sake of comparison to previous literature and to maximize the differences in dissolution, a rather high upper potential limit is used. Since we present online dissolution data, dissolution for cycles to lower potentials can be also extracted from the graphs. The most significant findings here are the drastic changes in the amount of dissolved material as well as the ratio of anodic (during forward going sweep of CV) to cathodic (during backward going sweep of CV) dissolution between the materials. As expected, bare Pt is much more stable than Pd, with an order of magnitude difference in the dissolution amount during a CV. The dissolved amount of PGM (both anodic and cathodic) decreases in the same order as the CeOx thickness increases and the same anodic and cathodic features are observed compared to bare metals. A direct comparison of bare Pd and the thickest Pd−Ce$_{20}$ sample reveals a 10-fold decrease in Pd dissolution, which is a sign of protection through the oxide film. An extensive analysis of each sample's dissolution behavior is presented in Table S4. For the thickest CeO$_x$ layer, we observe a shift of up to 280 mV to more positive values in the anodic dissolution onset potential.

Figure S7 shows the lack of any measurable Ce dissolution of the thickest CeO$_x$ films. Thus, even the film with the highest amount of Ce present does not reach sufficient Ce species in the electrolyte to pass the ICP-MS' detection limit of ca. 1 pg cm^{-2} s^{-1}. This is in line with the thermodynamics of Ce, which predicts a window of Ce(OH)$_3$ stability above a pH of 11.4 (calculated using the detection limit of Ce) between −2.05 and 1.56 V$_{RHE}$.[1]

A graphical overview of the most important findings of the electrochemical activity and stability measurements is shown in Figure 4. The activity of Pd increases gradually, while its
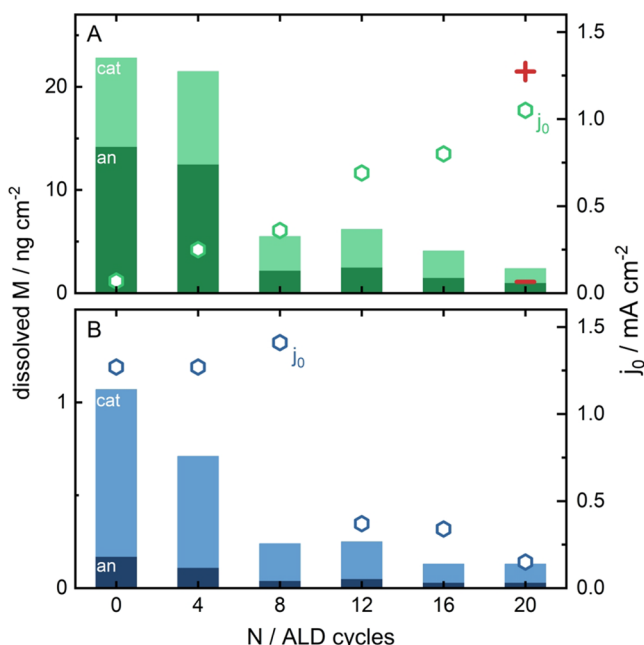
Figure 4. Summary of the sample's HOR activity in terms of j_0 (hexagons) and the dissolved M (anodic: solid-, cathodic: pale-bars) of Pd (A) and Pt (B). The red plus (j_0) and minus (dissolved M) signs represent the data of the benchmark Pt_0 within the Pd plot.

dissolution decreases drastically at ≥8 ALD cycles. Pt shows a similar decrease in dissolution at 8 ALD cycles and this coverage exhibits the highest j_0 on Pt, which is a 10% improvement over bare Pt. We want to emphasize the y-scale highlighting the order of magnitude difference in dissolution between Pd and Pt. However, the effect of the CeO_x layer renders Pd covered by 20 ALD cycles almost as active and stable as the benchmark Pt (red markers in Figure 4A).

■ DISCUSSION

In literature, the improved HOR activity of Pd-CeO_x systems is typically attributed to the beneficial alteration of the Pd oxidation state by neighboring CeO_x.[50] However, the ex situ XPS results presented in this work are in contrast to this hypothesis: The oxidation state of the underlying PGM stays intact with increasing CeO_x coverage. On the other hand, the electrocatalytic HOR activity of the CeO_x covered Pd increases drastically with oxide coverage. Thus, for the most active CeO_x@Pd with 20 ALD layers, $E_{1/2}$ decreases by more than 300 mV and j_0 increases 15 times, almost reaching those of a pure Pt benchmark. The HOR activity of Pt-CeO_x improves to a lower extent with the addition of small amounts of CeO_x.

As depicted in Figure 5, we support the theory that a direct interface between CeO_x and Pd^0 is responsible for the catalyst activation (Figure 5). Thermodynamically, the alkaline environment favors $Ce(OH)_3$ species, which might form in situ on the surface of CeO_x during the HOR. This interface serves as a source of OH^-, which is required for the HOR in alkaline media and, thus, facilitates the oxidative desorption Volmer step by supplying OH^- to a nearby strongly bound H_{ad} site on Pd.[24,51] Therefore, the interface process can be described as a bifunctional mechanism where Pd is mitigating dissociative H adsorption and CeO_x provides the OH^-. By accelerating the desorption of strongly adsorbed H, the PdH_x
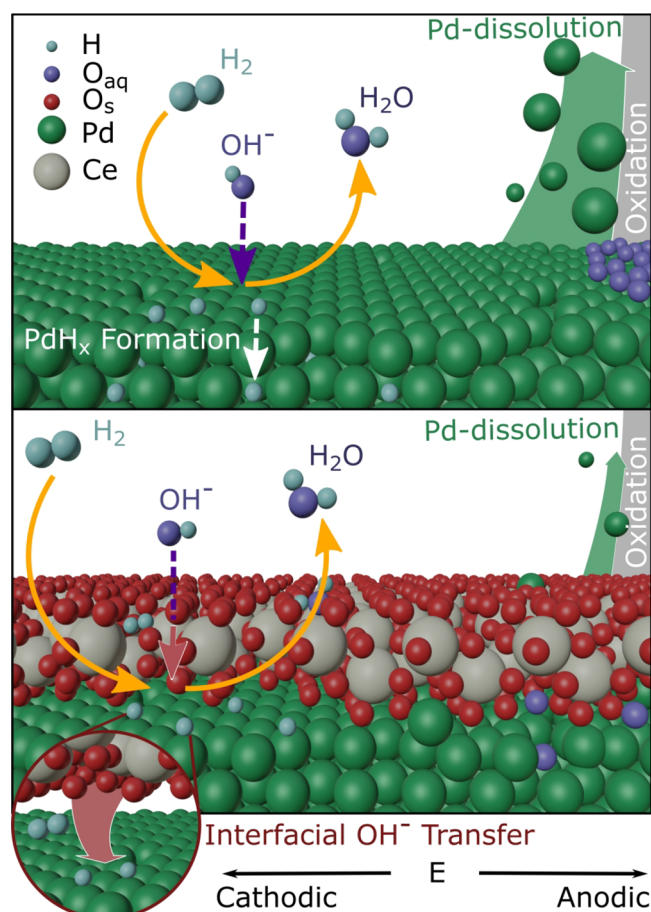

Figure 5. Schematic of electrochemical processes at Pd (A) and the Pd-CeO_x interface (B). The capability of CeO_x to transfer oxygen species directly to the adsorbed H (inset), facilitates the Volmer step at low potentials and hinders PdH_x formation.

formation is suppressed, which is evidenced by a significant shift in HOR onset potential.

Besides the activation of electrocatalysts, this work addresses the stabilization of modified Pd and Pt electrocatalysts. In line with previous reports on buried interfaces,[30,32,36] we show that the ORR activity is decreasing with increasing thickness of CeO_x, which is attributed to a semipermeable character of the CeO_x layer. The dissolution of the catalyst is consequently also affected, since mass transport within such layers is controlled by the size of the diffusing species.[34] This assumption is confirmed by online dissolution measurements, which show that, by increasing the CeO_x layer thickness, the protection of the PGMs toward dissolution improves. Thus, at higher CeO_x coverages, dissolution of Pd decreases by 1 order of magnitude, rendering it as stable as Pt. Moreover, the onset of dissolution shifts by ca. 300 mV to more positive potentials. These results can be explained by two phenomena. First, the surface layer of CeO_x hinders the PGM surface from being oxidized and shifts the thermodynamic oxidation to higher potentials.[30] This statement is confirmed by CVs (Figure S8), where the redox features of Pd are less intense and shifted further apart with increasing CeO_x layer thickness. Second, the porous CeO_x layer blocks the transiently dissolved ions from entering the bulk electrolyte. Therefore, the small amount of dissolved PGM reaches the ICP-MS' at a later point in time.

CONCLUSIONS

In an effort to unravel the role of an oxophilic layer on the HOR activity of platinum group metals, we prepared and investigated CeO_x covered Pt and Pd model electrocatalysts. With the help of numerous surface science methods, it was demonstrated that porous CeO_x layers of different thicknesses were successfully formed. The electrochemical activity and dissolution stability were studied with rotating disk electrode and online inductively coupled plasma mass spectrometry, respectively. It was found that the presence and variation of the CeO_x layer thickness do not affect the PGM oxidation state. Instead, the 15-fold increase in the exchange current density of the HOR is presumably due to OH^- supply to the catalyst facilitated by the oxide overlayer. The observed order of magnitude decrease in Pt and Pd dissolution was explained by the hindered mass-transfer of Pt/Pd ions within the semipermeable oxide layer. This hypothesis was supported by using oxygen reduction as a probe reaction. Moreover, it was shown that CeO_x is practically insoluble in the studied potentials and pHs. As a direct outcome of this study, the application of high-surface-area Pd-CeO_x core−shell nanoparticles with maximized catalyst-oxide interface is suggested as an ideal morphology to improve the performance of AEMFC anodes.

ASSOCIATED CONTENT

Ⓢ Supporting Information

The Supporting Information is available free of charge at https://pubs.acs.org/doi/10.1021/acs.chemmater.0c02048.

Schematic of experimental procedures, additional XPS analysis and discussion, spectroscopic ellipsometric data, AFM data, additional electrochemical activity, and stability data (PDF)

AUTHOR INFORMATION

Corresponding Authors

Florian D. Speck − Helmholtz-Institute Erlangen-Nürnberg for Renewable Energy (IEK-11), Forschungszentrum Jülich GmbH, 91058 Erlangen, Germany; Department of Chemical and Biological Engineering, Friedrich-Alexander-Universität Erlangen-Nürnberg, 91058 Erlangen, Germany; orcid.org/0000-0002-7649-9261; Email: f.speck@fz-juelich.de

Serhiy Cherevko − Helmholtz-Institute Erlangen-Nürnberg for Renewable Energy (IEK-11), Forschungszentrum Jülich GmbH, 91058 Erlangen, Germany; orcid.org/0000-0002-7188-4857; Email: s.cherevko@fz-juelich.de

Authors

Farhan S. M. Ali − Department of Chemistry and Materials Science, Aalto University School of Chemical Engineering, FI 00076 Aalto, Finland

Michael T. Y. Paul − Helmholtz-Institute Erlangen-Nürnberg for Renewable Energy (IEK-11), Forschungszentrum Jülich GmbH, 91058 Erlangen, Germany

Ramesh K. Singh − The Wolfson Department of Chemical Engineering, Technion−Israel Institute of Technology, 3200003 Haifa, Israel; The Nancy & Stephen Grand Technion Energy Program (GTEP), Technion - Israel Institute of Technology, 3200003 Haifa, Israel

Thomas Böhm − Helmholtz-Institute Erlangen-Nürnberg for Renewable Energy (IEK-11), Forschungszentrum Jülich GmbH, 91058 Erlangen, Germany; Department of Chemical and Biological Engineering, Friedrich-Alexander-Universität Erlangen-Nürnberg, 91058 Erlangen, Germany; orcid.org/0000-0003-2036-2159

André Hofer − Department of Chemistry and Pharmacy, Friedrich-Alexander-Universität Erlangen-Nürnberg, Chemistry of Thin Film Materials, IZNF, 91058 Erlangen, Germany

Olga Kasian − Helmholtz-Zentrum Berlin GmbH, Helmholtz-Institute Erlangen-Nuernberg, 14109 Berlin, Germany; orcid.org/0000-0001-6315-0637

Simon Thiele − Helmholtz-Institute Erlangen-Nürnberg for Renewable Energy (IEK-11), Forschungszentrum Jülich GmbH, 91058 Erlangen, Germany; Department of Chemical and Biological Engineering, Friedrich-Alexander-Universität Erlangen-Nürnberg, 91058 Erlangen, Germany; orcid.org/0000-0002-9526-2286

Julien Bachmann − Department of Chemistry and Pharmacy, Friedrich-Alexander-Universität Erlangen-Nürnberg, Chemistry of Thin Film Materials, IZNF, 91058 Erlangen, Germany; Institute of Chemistry, Saint Petersburg State University, 198504 Saint Petersburg, Russian Federation; orcid.org/0000-0001-6480-6212

Dario R. Dekel − The Wolfson Department of Chemical Engineering, Technion−Israel Institute of Technology, 3200003 Haifa, Israel; The Nancy & Stephen Grand Technion Energy Program (GTEP), Technion - Israel Institute of Technology, 3200003 Haifa, Israel; orcid.org/0000-0002-8610-0808

Tanja Kallio − Department of Chemistry and Materials Science, Aalto University School of Chemical Engineering, FI 00076 Aalto, Finland; orcid.org/0000-0001-6671-8582

Complete contact information is available at:
https://pubs.acs.org/10.1021/acs.chemmater.0c02048

Notes

The authors declare no competing financial interest.

REFERENCES

(1) Pourbaix, M. Atlas of Electrochemical Equilibria in Aqueous Solutions; NACE International, 1974.

(2) Varcoe, J. R.; Atanassov, P.; Dekel, D. R.; Herring, A. M.; Hickner, M. A.; Kohl, P. A.; Kucernak, A. R.; Mustain, W. E.; Nijmeijer, K.; Scott, K.; Xu, T.; Zhuang, L.; et al. Anion-Exchange Membranes in Electrochemical Energy Systems. Energy Environ. Sci. 2014, 7, 3135−3191.

(3) Rheinlander, P.; Henning, S.; Herranz, J.; Gasteiger, H. A. Comparing Hydrogen Oxidation and Evolution Reaction Kinetics on Polycrystalline Platinum in 0.1 and 1 M KOH. ECS Trans. 2013, 50, 2163−2174.

pubs.acs.org/cm

(4) Dekel, D. R. Review of Cell Performance in Anion Exchange Membrane Fuel Cells. *J. Power Sources* **2018**, *375*, 158−169.

(5) Dekel, D. R. Unraveling Mysteries of Hydrogen Electrooxidation in Anion Exchange Membrane Fuel Cells. *Curr. Opin. Electrochem.* **2018**, *12*, 182−188.

(6) Santori, P. G.; Speck, F. D.; Li, J.; Zitolo, A.; Jia, Q. Y.; Mukerjee, S.; Cherevko, S.; Jaouen, F. Effect of Pyrolysis Atmosphere and Electrolyte pH on the Oxygen Reduction Activity, Stability and Spectroscopic Signature of FeN$_x$ Moieties in Fe-N-C Catalysts. *J. Electrochem. Soc.* **2019**, *166*, F3311−F3320.

(7) Martinez, U.; Komini Babu, S.; Holby, E. F.; Zelenay, P. Durability Challenges and Perspective in the Development of PGM-Free Electrocatalysts for the Oxygen Reduction Reaction. *Curr. Opin. Electrochem.* **2018**, *9*, 224−232.

(8) Speck, F. D.; Santori, P. G.; Jaouen, F.; Cherevko, S. Mechanisms of Manganese Oxide Electrocatalysts Degradation During Oxygen Reduction and Oxygen Evolution Reactions. *J. Phys. Chem. C* **2019**, *123*, 25267−25277.

(9) Davydova, E. S.; Mukerjee, S.; Jaouen, F.; Dekel, D. R. Electrocatalysts for Hydrogen Oxidation Reaction in Alkaline Electrolytes. *ACS Catal.* **2018**, *8*, 6665−6690.

(10) Roy, A.; Talarposhti, M. R.; Normile, S. J.; Zenyuk, I. V.; De Andrade, V.; Artyushkova, K.; Serov, A.; Atanassov, P. Nickel−Copper Supported on a Carbon Black Hydrogen Oxidation Catalyst Integrated into an Anion-Exchange Membrane Fuel Cell. *Sustainable Energy Fuels* **2018**, *2*, 2268−2275.

(11) Sheng, W.; Bivens, A. P.; Myint, M.; Zhuang, Z.; Forest, R. V.; Fang, Q.; Chen, J. G.; Yan, Y. Non-Precious Metal Electrocatalysts with High Activity for Hydrogen Oxidation Reaction in Alkaline Electrolytes. *Energy Environ. Sci.* **2014**, *7*, 1719−1724.

(12) Davydova, E.; Zaffran, J.; Dhaka, K.; Toroker, M.; Dekel, D. Hydrogen Oxidation on Ni-Based Electrocatalysts: The Effect of Metal Doping. *Catalysts* **2018**, *8*, 454−473.

(13) Davydova, E. S.; Speck, F. D.; Paul, M. T. Y.; Dekel, D. R.; Cherevko, S. Stability Limits of Ni-Based Hydrogen Oxidation Electrocatalysts for Anion Exchange Membrane Fuel Cells. *ACS Catal.* **2019**, *9*, 6837−6845.

(14) Parsons, R. The Rate of Electrolytic Hydrogen Evolution and the Heat of Adsorption of Hydrogen. *Trans. Faraday Soc.* **1958**, *54*, 1053−1063.

(15) Trasatti, S. Work Function, Electronegativity, and Electrochemical Behaviour of Metals. *J. Electroanal. Chem. Interfacial Electrochem.* **1972**, *39*, 163−184.

(16) Zeradjanin, A. R.; Grote, J.-P.; Polymeros, G.; Mayrhofer, K. J. J. A Critical Review on Hydrogen Evolution Electrocatalysis: Re-Exploring the Volcano-Relationship. *Electroanalysis* **2016**, *28*, 2256−2269.

(17) Durst, J.; Simon, C.; Hasché, F.; Gasteiger, H. A. Hydrogen Oxidation and Evolution Reaction Kinetics on Carbon Supported Pt, Ir, Rh, and Pd Electrocatalysts in Acidic Media. *J. Electrochem. Soc.* **2015**, *162*, F190−F203.

(18) Sheng, W.; Gasteiger, H. A.; Shao-Horn, Y. Hydrogen Oxidation and Evolution Reaction Kinetics on Platinum: Acid Vs Alkaline Electrolytes. *J. Electrochem. Soc.* **2010**, *157*, B1529.

(19) Omasta, T. J.; Peng, X.; Miller, H. A.; Vizza, F.; Wang, L.; Varcoe, J. R.; Dekel, D. R.; Mustain, W. E. Beyond 1.0 W cm^{-2} performance without Platinum: The Beginning of a New Era in Anion Exchange Membrane Fuel Cells. *J. Electrochem. Soc.* **2018**, *165*, J3039−J3044.

(20) Peng, X.; Omasta, T. J.; Magliocca, E.; Wang, L.; Varcoe, J. R.; Mustain, W. E. Nitrogen-Doped Carbon-CoO$_x$ Nanohybrids: A Precious Metal Free Cathode That Exceeds 1.0 W cm^{-2} Peak Power and 100 h Life in Anion-Exchange Membrane Fuel Cells. *Angew. Chem., Int. Ed.* **2019**, *58*, 1046−1051.

(21) Cherevko, S.; Zeradjanin, A. R.; Keeley, G. P.; Mayrhofer, K. J. J. A Comparative Study on Gold and Platinum Dissolution in Acidic and Alkaline Media. *J. Electrochem. Soc.* **2014**, *161*, H822−H830.

(22) Schalenbach, M.; Kasian, O.; Ledendecker, M.; Speck, F. D.; Mingers, A. M.; Mayrhofer, K. J. J.; Cherevko, S. The Electrochemical Dissolution of Noble Metals in Alkaline Media. *Electrocatalysis* **2018**, *9*, 153−161.

(23) Strmcnik, D.; Uchimura, M.; Wang, C.; Subbaraman, R.; Danilovic, N.; van der Vliet, D.; Paulikas, A. P.; Stamenkovic, V. R.; Markovic, N. M. Improving the Hydrogen Oxidation Reaction Rate by Promotion of Hydroxyl Adsorption. *Nat. Chem.* **2013**, *5*, 300−306.

(24) Miller, H. A.; Lavacchi, A.; Vizza, F.; Marelli, M.; Di Benedetto, F.; D'Acapito, F.; Paska, Y.; Page, M.; Dekel, D. R. A Pd/C-CeO$_2$ Anode Catalyst for High-Performance Platinum-Free Anion Exchange Membrane Fuel Cells. *Angew. Chem., Int. Ed.* **2016**, *55*, 6004−6007.

(25) Miller, H. A.; et al. Highly Active Nanostructured Palladium-Ceria Electrocatalysts for the Hydrogen Oxidation Reaction in Alkaline Medium. *Nano Energy* **2017**, *33*, 293−305.

(26) Yu, H.; Davydova, E. S.; Ash, U.; Miller, H. A.; Bonville, L.; Dekel, D. R.; Maric, R. Palladium-Ceria Nanocatalyst for Hydrogen Oxidation in Alkaline Media: Optimization of the Pd−CeO$_2$ Interface. *Nano Energy* **2019**, *57*, 820−826.

(27) Fu, J.; et al. Constructing Pd/CeO$_2$/C to Achieve High Leaching Resistance and Activity for Catalytic Wet Air Oxidation of Aqueous Amide. *ACS Catal.* **2018**, *8*, 4980−4985.

(28) Yarmiayev, V.; Alesker, M.; Muzikansky, A.; Zysler, M.; Zitoun, D. Enhancement of Palladium HOR Activity in Alkaline Conditions through Ceria Surface Doping. *J. Electrochem. Soc.* **2019**, *166*, F3234−F3239.

(29) Ralbag, N.; Davydova, E. S.; Mann-Lahav, M.; Cong, P.; He, J.; Beale, A. M.; Grader, G. S.; Avnir, D.; Dekel, D. R. Ceria Entrapped Palladium Novel Composites for Hydrogen Oxidation Reaction in Alkaline Medium. *J. Electrochem. Soc.* **2020**, *167*, 054514.

(30) Stühmeier, B. M.; Selve, S.; Patel, M. U. M.; Geppert, T. N.; Gasteiger, H. A.; El-Sayed, H. A. Highly Selective Pt/TiO$_x$ Catalysts for the Hydrogen Oxidation Reaction. *ACS Appl. Energy Mater.* **2019**, *2*, 5534−5539.

(31) Maeda, K.; Teramura, K.; Lu, D.; Saito, N.; Inoue, Y.; Domen, K. Roles of Rh/Cr$_2$O$_3$(Core/Shell) Nanoparticles Photodeposited on Visible-Light-Responsive (Ga$_{1-X}$Zn$_x$)(N$_{1-X}$O$_x$) Solid Solutions in Photocatalytic Overall Water Splitting. *J. Phys. Chem. C* **2007**, *111*, 7554−7560.

(32) Genorio, B.; Strmcnik, D.; Subbaraman, R.; Tripkovic, D.; Karapetrov, G.; Stamenkovic, V. R.; Pejovnik, S.; Markovic, N. M. Selective Catalysts for the Hydrogen Oxidation and Oxygen Reduction Reactions by Patterning of Platinum with Calix[4]Arene Molecules. *Nat. Mater.* **2010**, *9*, 998−1003.

(33) Yun, S. W.; Park, S. A.; Kim, T. J.; Kim, J. H.; Pak, G. W.; Kim, Y. T. Hydrogen Oxidation-Selective Electrocatalysis by Fine Tuning of Pt Ensemble Sites to Enhance the Durability of Automotive Fuel Cells. *ChemSusChem* **2017**, *10*, 489−493.

(34) Esposito, D. V. Membrane-Coated Electrocatalysts—an Alternative Approach to Achieving Stable and Tunable Electrocatalysis. *ACS Catal.* **2018**, *8*, 457−465.

(35) Maeda, K.; Sakamoto, N.; Ikeda, T.; Ohtsuka, H.; Xiong, A.; Lu, D.; Kanehara, M.; Teranishi, T.; Domen, K. Preparation of Core-Shell-Structured Nanoparticles (with a Noble-Metal or Metal Oxide Core and a Chromia Shell) and Their Application in Water Splitting by Means of Visible Light. *Chem. - Eur. J.* **2010**, *16*, 7750−7759.

(36) Takata, T.; Pan, C.; Nakabayashi, M.; Shibata, N.; Domen, K. Fabrication of a Core-Shell-Type Photocatalyst Via Photodeposition of Group Iv and V Transition Metal Oxyhydroxides: An Effective Surface Modification Method for Overall Water Splitting. *J. Am. Chem. Soc.* **2015**, *137*, 9627−9634.

(37) Hornberger, E.; Bergmann, A.; Schmies, H.; Kuhl, S.; Wang, G.; Drnec, J.; Sandbeck, D. J. S.; Ramani, V.; Cherevko, S.; Mayrhofer, K. J. J.; Strasser, P.; et al. In Situ Stability Studies of Platinum Nanoparticles Supported on Ruthenium−Titanium Mixed Oxide (RTO) for Fuel Cell Cathodes. *ACS Catal.* **2018**, *8*, 9675−9683.

(38) Schmies, H.; et al. Unravelling Degradation Pathways of Oxide-Supported Pt Fuel Cell Nanocatalysts under in Situ Operating Conditions. *Adv. Energy Mater.* **2018**, *8*, 1701663.

(39) George, M.; Zhang, G. R.; Schmitt, N.; Brunnengraber, K.; Sandbeck, D. J. S.; Mayrhofer, K. J. J.; Cherevko, S.; Etzold, B. J. M.

Effect of Ionic Liquid Modification on the ORR Performance and Degradation Mechanism of Trimetallic Ptnimo/C Catalysts. *ACS Catal.* **2019**, *9*, 8682−8692.

(40) Zhang, G. R.; Wolker, T.; Sandbeck, D. J. S.; Munoz, M.; Mayrhofer, K. J. J.; Cherevko, S.; Etzold, B. J. M. Tuning the Electrocatalytic Performance of Ionic Liquid Modified Pt Catalysts for the Oxygen Reduction Reaction Via Cationic Chain Engineering. *ACS Catal.* **2018**, *8*, 8244−8254.

(41) Pohl, M. D.; Haschke, S.; Göhl, D.; Kasian, O.; Bachmann, J.; Mayrhofer, K. J. J.; Katsounaros, I. Extension of the Rotating Disk Electrode Method to Thin Samples of Non-Disk Shape. *J. Electrochem. Soc.* **2019**, *166*, H791−H794.

(42) Klemm, S. O.; Topalov, A. A.; Laska, C. A.; Mayrhofer, K. J. J. Coupling of a High Throughput Microelectrochemical Cell with Online Multielemental Trace Analysis by ICP-MS. *Electrochem. Commun.* **2011**, *13*, 1533−1535.

(43) Zhang, F.; Wang, P.; Koberstein, J.; Khalid, S.; Chan, S.-W. Cerium Oxidation State in Ceria Nanoparticles Studied with X-Ray Photoelectron Spectroscopy and Absorption near Edge Spectroscopy. *Surf. Sci.* **2004**, *563*, 74−82.

(44) Holgado, J. P.; Munuera, G.; Espinós, J. P.; González-Elipe, A. R. Xps Study of Oxidation Processes of CeOx Defective Layers. *Appl. Surf. Sci.* **2000**, *158*, 164−171.

(45) Marković, N. M.; Sarraf, S. T.; Gasteiger, H. A.; Ross, P. N. Hydrogen Electrochemistry on Platinum Low-Index Single-Crystal Surfaces in Alkaline Solution. *J. Chem. Soc., Faraday Trans.* **1996**, *92*, 3719−3725.

(46) Campos-Roldán, C. A.; González-Huerta, R. G.; Alonso-Vante, N. Experimental Protocol for HOR and ORR in Alkaline Electrochemical Measurements. *J. Electrochem. Soc.* **2018**, *165*, J3001−J3007.

(47) Durst, J.; Siebel, A.; Simon, C.; Hasché, F.; Herranz, J.; Gasteiger, H. A. New Insights into the Electrochemical Hydrogen Oxidation and Evolution Reaction Mechanism. *Energy Environ. Sci.* **2014**, *7*, 2255.

(48) Cherevko, S.; Zeradjanin, A. R.; Topalov, A. A.; Kulyk, N.; Katsounaros, I.; Mayrhofer, K. J. J. Dissolution of Noble Metals During Oxygen Evolution in Acidic Media. *ChemCatChem* **2014**, *6*, 2219−2223.

(49) Burke, L. D.; Casey, J. K. The Electrocatalytic Behaviour of Palladium in Acid and Base. *J. Appl. Electrochem.* **1993**, *23*, 573−582.

(50) Zhou, Y.; Lawrence, N. J.; Wu, T.-S.; Liu, J.; Kent, P.; Soo, Y.-L.; Cheung, C. L. Pd/CeO$_{2-X}$ nanorod Catalysts for CO Oxidation: Insights into the Origin of Their Regenerative Ability at Room Temperature. *ChemCatChem* **2014**, *6*, 2937−2946.

(51) Alesker, M.; Page, M.; Shviro, M.; Paska, Y.; Gershinsky, G.; Dekel, D. R.; Zitoun, D. Palladium/Nickel Bifunctional Electrocatalyst for Hydrogen Oxidation Reaction in Alkaline Membrane Fuel Cell. *J. Power Sources* **2016**, *304*, 332−339.